Open access • Journal Article • DOI:10.1021/ACS.IECR.6B00963

Deactivation Study of Fe2O3–CeO2 during Redox Cycles for CO Production from CO2 — Source link

N. V. R. Aditya Dharanipragada, Maria Meledina, Vladimir Galvita, Hilde Poelman ...+4 more authors

Institutions: Ghent University, University of Antwerp

Published on: 13 May 2016 - Industrial & Engineering Chemistry Research (American Chemical Society)

Topics: Oxygen storage and Redox

Deactivation study of $Fe_2O_3-CeO_2$ during redox cycles for CO production from CO_2

Reference:

Dharanipragada N. V. R. Aditya, Meledina Maria, Galvita Vladimir V., Poelman Hilde, Turner Stuart, Van Tendeloo Gustaaf, Detavernier Christophe, Marin Guy B..- Deactivation study of $Fe_2O_3-CeO_2$ during redox cycles for CO production from CO_2
Industrial and engineering chemistry research - ISSN 0888-5885 - 55:20(2016), p. 5911-5922
Full text (Publishers DOI): http://dx.doi.org/doi:10.1021/acs.iecr.6b00963
To cite this reference: http://hdl.handle.net/10067/1342140151162165141

I&EC research
Industrial & Engineering Chemistry Research

Article

Deactivation study of Fe2O3-CeO2 during redox cycles for CO production from CO2

Naga Venkata Ranga Aditya Dharanipragada, Maria Meledina, Vladimir V. Galvita, Hilde Poelman, Stuart Turner, Gustaaf Van Tendeloo, Christophe Detavernier, and Guy B Marin

Ind. Eng. Chem. Res., **Just Accepted Manuscript** • DOI: 10.1021/acs.iecr.6b00963 • Publication Date (Web): 22 Apr 2016

ACS Publications

Industrial & Engineering Chemistry Research is published by the American Chemical Society. 1155 Sixteenth Street N.W., Washington, DC 20036

Deactivation study of Fe_2O_3-CeO_2 during redox cycles for CO production from CO_2

N.V.R. Aditya Dharanipragada[a], Maria Meledina[b], Vladimir V. Galvita[a], Hilde Poelman[a], Stuart Turner[b], Gustaaf Van Tendeloo[b], Christophe Detavernier[c], and Guy B. Marin[a]*

[a]Laboratory for Chemical Technology, Ghent University, Technologiepark 914, B-9052 Gent, Belgium.

[b]Electron Microscopy for Materials Science (EMAT), Department of Physics, University of Antwerp, Groenenborgerlaan 171, B-2020 Antwerp, Belgium.

[c]Department of Solid State Sciences, Ghent University, Krijgslaan 281, S1, B-9000 Ghent, Belgium

[*]Corresponding author: E-mail address: Vladimir.Galvita@Ugent.be

Abstract

Deactivation was investigated in Fe_2O_3-CeO_2 oxygen storage materials during repeated H_2-reduction and CO_2-reoxidation. In situ XRD, XAS and TEM were used to identify phases, crystallite sizes and morphological changes upon cycling operation. The effect of redox cycling was investigated both in Fe-rich (80wt% Fe_2O_3-CeO_2) and Ce-rich (10wt%Fe_2O_3-CeO_2) materials. The former consisted of 100nm Fe_2O_3 particles decorated with 5-10nm $Ce_{1-x}Fe_xO_{2-x}$. The latter presented CeO_2 with incorporated Fe, i.e. a solid solution of $Ce_{1-x}Fe_xO_{2-x}$, as main oxygen carrier. By modelling the EXAFS Ce-K signal for as prepared 10wt%Fe_2O_3-CeO_2, the amount of Fe in CeO_2 was determined as 21mol%, corresponding to 86% of the total iron content. Sintering and solid-solid transformations, the latter including both new phase formation and element segregation, were identified as deactivation pathways upon redox cycling. In Ce-rich material, perovskite ($CeFeO_3$) was identified by XRD. This phase remained inert during reduction and reoxidation, resulting in an overall lower oxygen storage capacity. Further, Fe segregated from the solid solution, thereby decreasing its reducibility. In addition, an increase in crystallite size occurred for all phases. In Fe-rich material, sintering is the main deactivation pathway, although Fe segregation from the solid solution and perovskite formation cannot be excluded.

Keywords: Deactivation, Sintering, solid-solid transformation, in situ XRD, XAS.

1.0 Introduction

With rising global temperatures, the necessity to reduce greenhouse gas emissions like CO_2 has only gained significance. Several technologies have been proposed to minimize CO_2 emissions[1-3]. One such technology, which can utilize directly CO_2 by converting it to value added fuels is chemical looping[4-6], a cyclic redox process based on the regeneration of oxygen storage materials. In the first half-cycle, gases such as CH_4 are employed to reduce the oxygen storage material, resulting in the production of CO_2 and H_2O. The latter are used in the second half-cycle for the regeneration of the oxygen storage material. When CO_2 is used as reoxidation agent this results in the production of CO, which is a useful raw material, e.g. for Fischer-Tropsch processes. Since the amount of CO_2 utilized in the second step is much higher than produced in the first step, the process is termed CO_2 utilization[7, 8].

The process economics of chemical looping are limited by the stability of the oxygen storage materials. There are many paths towards the deactivation of oxygen storage materials. For example, a material may be poisoned by a contaminant present in the reducing or oxidizing agents. Its surface, pores and voids may be fouled by carbon produced during cracking/condensation if hydrocarbon or carbon monoxide reactants are used for reduction. Due to the high temperature of operation in chemical looping (T > 650°C), thermal degradation may occur in the form of active phase crystallite growth, i.e. sintering, collapse of the pore structure and/or solid-state reactions of the active phase with the carrier or modifying element. Hence, the choice of oxygen storage material and modifying element towards chemical looping play a crucial role.

Oxides of transition metals, such as Ni, Cu, Mo and Fe, are typically used as oxygen carriers. Among these, iron oxides stand out because of their natural abundance and high reoxidation capacity with CO_2 over a wide range of operating conditions (700°C -1000°C)[9-11]. However, pure iron oxides tend to deactivate rapidly. The major factor for deactivation in pure iron oxide materials is sintering[12-13].

To overcome this challenge, iron oxides are often modified with other oxide materials, e.g. CeO_2[14, 15], $CeZrO_2$[16], MgO[17], Al_2O_3[18, 19], ZrO_2[20], SiO_2[21], TiO_2[22] and $MgAl_2O_4$[24-26]. These promoter materials prevent contact between adjacent iron oxide particles, resulting in relatively stable particle size, and are therefore termed as physical textural promoters. They mitigate sintering by acting as a physical barrier. However, during a prolonged cyclic process, some promoters can undergo solid-solid transformations with iron oxide, e.g. MgO to $MgFe_2O_4$, Al_2O_3

to $FeAl_2O_4$ and CeO_2 to perovskite ($CeFeO_3$). These new phases continue to prevent sintering by providing a physical barrier between adjacent iron oxide particles, but reduce the total oxygen storage capacity because the iron oxide involved in solid-solid transformations no longer contributes. For Fe_2O_3 with Al_2O_3, iron oxide deactivates significantly during the progression of the redox cycles due to its solid−solid transformation to $FeAl_2O_4$, requiring a higher temperature of reduction and reoxidation. Hence, the success of these promoters greatly depends on the nature of these transformations.

Certain promoters contribute towards the redox reaction, along with iron oxide, in addition to providing a physical barrier. These are therefore termed chemically active promoters, e.g. CeO_2, $CeZrO_2$[16, 27]among the latter, CeO_2 stands out as it has high activity towards methane oxidation by lattice oxygen, as well as reasonable H_2O or CO_2 reoxidation capacity[28, 29]. The redox couple Ce^{4+} and Ce^{3+} facilitates oxygen storage and release from its bulk fluorite lattice. Additionally, CeO_2 induces structural modification and stabilization of iron oxides, making it an ideal candidate for promoting iron oxide in a chemical looping process. Indeed, the formation of a solid solution between CeO_2 and MeO_x (Me= Mn, Fe, or Cu) has been found to be responsible for enhanced reducibility at lower temperatures compared with pure CeO_2[8].

In a previous study, the influence of CeO_2 as chemically active promoter for iron oxides was investigated for a range of loadings. The addition of CeO_2 to Fe_2O_3 resulted in higher activity in comparison to the bulk oxides[8]. Among these mixed oxide materials, 80wt%Fe_2O_3-CeO_2 showed the highest redox properties. Despite its high initial activity, the material suffered from deactivation, albeit less severe than pure iron oxide. At the opposite side of the Fe_2O_3-CeO_2 mixing range 10wt%Fe_2O_3-CeO_2 and 30wt%Fe_2O_3-CeO_2 materials had low oxygen storage capacity but were less prone to deactivation.

The present investigation focuses on the origin and nature of deactivation in Fe_2O_3-rich and CeO_2-rich Fe_2O_3-CeO_2 materials. For this study, the most active 80wt%Fe_2O_3-CeO_2 was compared with 10wt%Fe_2O_3-CeO_2, where CeO_2 acts as bulk oxygen carrier material. The addition of a small amount of Fe_2O_3 to CeO_2 is known to result in lower CeO_2 redox temperatures, making this material applicable in chemical looping redox processes[8].

Mechanisms of deactivation such as sintering and solid-solid transformation during chemical looping were investigated using in situ XRD, TEM and XAS. In situ XRD was employed to study the redox properties during the reaction. XAS and TEM were employed to study the local environment around Fe and Ce.

2.0 Experimental

2.1 Material preparation

Fe_2O_3-CeO_2 materials with 10 and 80wt% Fe_2O_3 were prepared. The following chemicals were used as precursor materials for the synthesis of mixed oxides: $Fe(NO_3)_3.9H_2O$ (99.99+%, Sigma-Aldrich®) and $Ce(NO_3)_3.6H_2O$(99.99%,Sigma-Aldrich®). All samples were prepared via one pot co-precipitation by ammonium hydroxide. The precipitate was then separated by filtration, followed by drying in an oven at 120°C for 10 hours. The samples were calcined at 650°C for 6 hours.

In addition to the above materials, 50wt%Fe_2O_3-CeO_2 was synthesized by co-precipitation and subjected to 10 cycles of TPR-TPO up to a temperature of 950^{o}C as pre-treatment. This material was used for comparison of perovskite ($CeFeO_3$) redox properties with cycled materials.

The Brunauer–Emmett–Teller (BET) surface area of each sample was determined by N_2 adsorption at 77 K (five point BET method using Gemini Micromeritics). Prior to analysis, the sample was outgassed at 200 °C for 4 h to eliminate volatile adsorbates from the surface. The surface area of as prepared 10 and 80wt%Fe_2O_3-CeO_2 amounted to 18 m^2/g and 15 m^2/g respectively. The surface area of used samples decreased by ten times.

2.2 General characterization: X-Ray Diffraction (XRD)

The crystallographic phases of the materials were determined with a Siemens Diffractometer Kristalloflex D5000, with Cu Kα (λ=0.154nm) radiation. The powder patterns were collected in a 2θ range from 10° to 80° with a step of 0.02° and 30s counting time per angle. The crystallite size was determined using the Scherrer equation by fitting a Gaussian function to the three most intense characteristic peaks to obtain the peak width at half maximum.

2.3 X-Ray Absorption Spectroscopy (XAS)

XAS measurements were performed at the Fe-K (7112 eV), Ce-L_{III} (5873 eV) and Ce-K (40443 eV) edges. The Fe-K and Ce-L_{III} measurements were performed at the DUBBLE beam line (BM 26A) and the Ce-K edge data were collected at SNBL (BM 01B) both of the European Synchrotron Radiation Facility (ESRF) in Grenoble (France). The optics and energy alignment was performed using a Fe foil and CeO_2 reference.

2.4 EXAFS data reduction analysis

XAS data reduction and analysis were executed with Athena and Artemis, part of the Demeter 0.9.13 software package[30]. The pre-edge background was removed by subtracting an extrapolated modified Victoreen curve from the raw data. The edge energy E_0 was chosen at the maximum of the first derivative of the spectrum. The atomic background μ_o was calculated by the AUTOBK routine using a cubic spline fitting procedure. Background subtraction, normalization, $\chi(k)$ isolation and Fourier transformation were performed using the methodology of Koningsberger et al.[31]. In view of Ce-K edge EXAFS signal modelling, the amplitude reduction factor $S_o^2 = 0.83 \pm 0.05$ was calculated from reference CeO_2. The local environment of Ce was fitted by implementing a Fe doped CeO_2 model. The single scattering paths with significant contribution to the Ce-K signal were selected and used for further modelling.

The FEFF 6.0 ab initio code[32] was applied to calculate the phase shifts and backscattering amplitude functions of Ce–O, Ce–Ce and Ce–Fe contributions to the EXAFS signal. IFEFFIT was utilized for non-linear least-squares minimization of the objective function using a Levenberg–Marquardt algorithm, yielding estimates for the structural parameters[30]. For this minimization, multiple shell fitting was performed in R-space using multiple k-weightings. The fitting was performed by model discrimination of fit by implementing single scattering paths with and without incorporation of Fe. The agreement between model and experiment was evaluated statistically by means of the minimized objective function χ_v^2 and the F-value. The χ_v^2 is the reduced sum of square residuals with v degrees of freedom. The F-test was performed using Hamiltonian formulation[33] and the confidence interval α was calculated by the approach described by Bacchi et al.[34]. For global significance of the regression the inverse F-value or *R*-value is reported.

2.5 In situ XRD analysis

The crystallographic changes during H_2-TPR and CO_2-TPO were followed with in situ XRD in a home-built reaction chamber housed inside a Bruker-AXS D8 Discover apparatus (Cu Kα radiation of 0.154 nm) with a linear detector covering 20° in 2θ and an angular resolution of approximately 0.1° in 2θ. A typical collection time of 10 s was used during these experiments. 10 mg of powdered sample was evenly spread on a single crystal Si wafer. Interaction of the catalyst material with the Si wafer was never observed. After pump-down to a base pressure of 4 Pa, gases were supplied to the reactor chamber from a rig with calibrated mass flow meters.

A full XRD scan (10° to 65° with a step of 0.02°) was recorded at room temperature before and after each TPR and TPO experiment. The TPR was performed in flow conditions of H_2 at 1.1Nml/sec up to a temperature of 800°C. This was followed by reoxidation with CO_2 at the same flow rate up to 800°C. Both of these treatments were performed at a uniform heating rate of 20°C/min.

2.6 TEM

High angle annular dark field scanning transmission electron microscopy (HAADF-STEM), energy dispersive X-ray (EDX) spectroscopy and electron energy-loss spectroscopy (EELS) experiments were performed with a FEI Titan "cubed" electron microscope equipped with an aberration corrector for the probe-forming lens, a high resolution EELS spectrometer (Gatan GIF Quantum) and a wide solid angle "super-X" EDX detector, at 120 kV and 300 kV acceleration voltage. The STEM convergence semi-angle used was ~22 mrad, while the inner collection semi-angle for HAADF-STEM imaging at 300kV was ~50 mrad and at 120kV ~85 mrad.

2.7 Experimental Reactor Setup

Redox cycling measurements were carried out at atmospheric pressure in a quartz tube microreactor (i.d. 10 mm), placed in an electric furnace. Typically, 30 mg of material was packed in a quartz bed. This material was diluted with inert α-Al_2O_3 with a ratio of 1:10. The temperature of the catalyst bed was measured with K-type thermocouples touching the outside and inside of the reactor at the position of the catalyst bed. In all experiments, the material was reduced by H_2 and reoxidized by CO_2. In between He was purged during redox cyclic experiments. The total flow rate of the feed gas into the reactor was maintained constant at 1.1Nml/s by means of Brooks mass flow controllers. The redox property of the samples was investigated at 650°C. The feed and product gas streams were monitored online using an OmniStar Pfeiffer mass spectrometer (MS). The response of the MS detector was regularly verified with calibration gases. A carbon balance with a maximum deviation of 15% was obtained. The CO yield is calculated as (equation 1)

$$\text{Yield } (Y_i) = \frac{n_{CO}}{W} \qquad \text{(Eq. 1)}$$

where n_{CO} = Mole of CO produced (mol) ; W_{Fe} = Mass of oxygen carrier material [kg].

3.0 Results

3.1 Isothermal Cycling

The effect of redox cycling on the CO yield of 80wt%Fe_2O_3-CeO_2 and 10wt%Fe_2O_3-CeO_2 was studied at a temperature of 650°C during 100 redox cycles (Figure 1). The highest CO yield was shown by 80wt%Fe_2O_3-CeO_2. In this material the CO yield decreased steadily during the first 30 cycles and thereafter remained stable. For 10wt%Fe_2O_3-CeO_2, the CO yield steeply dropped during the first 10 cycles and then remained constant up to 100 cycles. Over the redox cycles, the conversion of CO_2 decreased from 15% to 6% for 80Fe-CeO_2 and from 9% to 2% for 10Fe-CeO_2. This decrease in CO yield for both materials is the result of deactivation. However, the different trends in decrease of CO yield (Figure 1) could suggest that different factors could govern the deactivation, determined by the interaction between the metal oxides present in both oxygen storage materials[13], possibly leading to different routes of deactivation. In order to identify the different mechanisms of deactivation, a systematic characterization of materials was performed to map out their redox properties in relation to their stability.

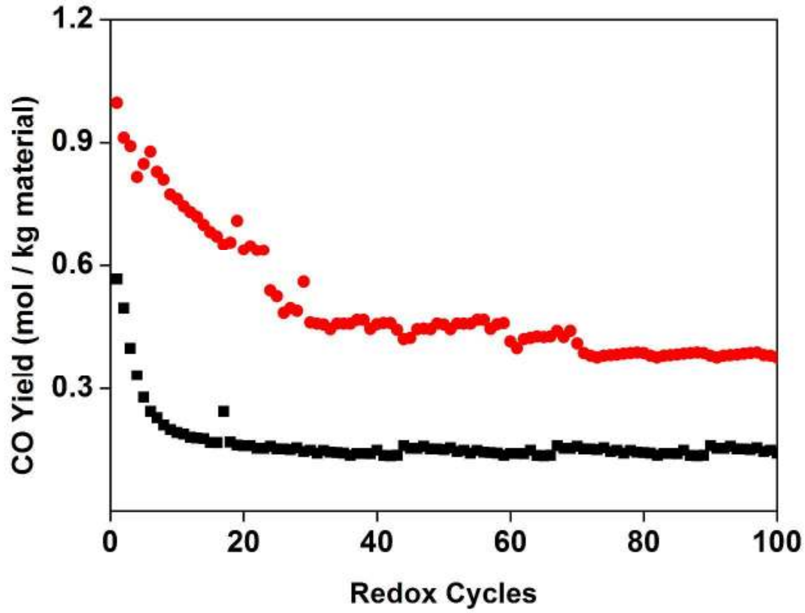

Figure 1: CO yield as a function of number of isothermal redox cycles for 10wt%Fe_2O_3-CeO_2 and 80wt%Fe_2O_3-CeO_2. (●) 80wt%Fe_2O_3-CeO_2 and (■) 10wt%Fe_2O_3-CeO_2.

3.2 Materials Characterization

3.2.1 XRD

The as prepared and cycled materials were characterized using XRD to identify the phases present. From the diffraction pattern of 80wt%Fe_2O_3-CeO_2 (Figure 2a (i)), characteristic peaks for Fe_2O_3 and CeO_2 were identified. For 10wt%Fe_2O_3-CeO_2 clear contributions of CeO_2 along with minor peaks of Fe_2O_3 (dotted lines) were observed (Figure 2a (ii)).

The state of the materials after redox cycling is shown in Figure 2b. The diffraction pattern of cycled 80wt%Fe_2O_3-CeO_2 (Figure 2b(i)) exhibited peaks at 2θ values corresponding to CeO_2 and Fe_3O_4. From the XRD of cycled 10wt%Fe_2O_3-CeO_2 (Figure 2b(ii)), peaks of CeO_2, Fe_3O_4 and perovskite ($CeFeO_3$) as new phase were identified. Further reoxidation to Fe_2O_3 can only be achieved if O_2/air is employed for reoxidation[35].

The crystallite sizes of the as prepared materials and 100 times cycled materials were calculated using the Scherrer equation (Table 1). For Fe_2O_3 in as prepared 80wt%Fe_2O_3-CeO_2 and Fe_3O_4 in both cycled materials, reliable values could be obtained from XRD. However, in as prepared 10wt%Fe_2O_3-CeO_2 the Fe_2O_3 diffractions were too weak for crystallite size determination. Hence, for the Fe_2O_3 phase in this material, crystallite sizes from TEM are reported in Table 1. The crystallite size of CeO_2 determined by XRD showed that crystallites in 10wt%Fe_2O_3-CeO_2 are larger than in 80wt%Fe_2O_3-CeO_2. In addition, the formation of a solid solution $Ce_{1-x}Fe_xO_{2-x}$ was identified from the lattice parameters of CeO_2 for both as prepared 10wt%Fe_2O_3-CeO_2 and 80wt%Fe_2O_3-CeO_2 (Table 1). The replacement of a larger cation (Ce^{+4}, 1.01 Å) with a smaller one (Fe^{+3}, 0.64 Å) led to contraction of the lattice and, hence, a smaller lattice parameter in comparison to pure CeO_2 (0.5411 nm)[8]. This is in agreement with the CeO_2 lattice parameter evolution for a series of 2wt% to 80wt%Fe_2O_3-CeO_2 (details of lattice parameter evolution for the series of materials in supplementary info Figure S1) and suggests that during synthesis, incorporation of Fe in CeO_2 occurred to form a solid solution $Ce_{1-x}Fe_xO_{2-x}$ which stabilized the crystallite size of CeO_2. The resulting solid solutions $Ce_{1-x}Fe_xO_{2-x}$ in both 10wt%Fe_2O_3-CeO_2 and 80wt%Fe_2O_3-CeO_2 are expected to present enhanced redox properties compared to pure CeO_2[16].

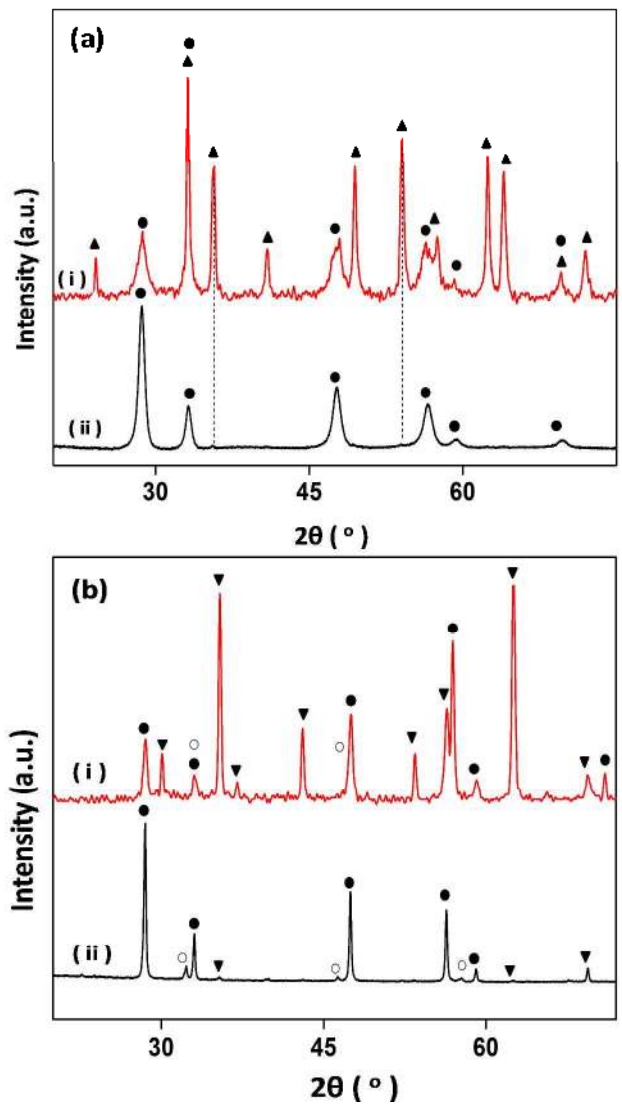

Figure 2: XRD diffraction patterns of (i) 80wt%Fe_2O_3-CeO_2 and (ii) 10wt%Fe_2O_3-CeO_2: a) as prepared and (b) 100 times cycled. (▲) Fe_2O_3, (●) CeO_2, (▼) Fe_3O_4, and (○) $CeFeO_3$.

After cycling, CeO_2 crystallites showed a 2.5 times increase in 10wt%Fe_2O_3-CeO_2 and 4 times increase in 80wt%Fe_2O_3-CeO_2. This was due to sintering of the oxygen storage material and segregation of incorporated Fe from the CeO_2 lattice, resulting in the formation of separate Fe_3O_4 phase. This phase segregation is also evidenced from the CeO_2 lattice parameters of cycled materials (Table 1) which were closer to that of pure CeO_2 (0.5411 nm), which indicates that part of the Fe was segregated upon cycling, leaving less Fe incorporated in the CeO_2 lattice.

Further, the new perovskite phase $CeFeO_3$ formed in 10wt%Fe_2O_3-CeO_2 upon cycling, also displayed large crystallite sizes (Table 1). Crystallites of pure iron oxide also suffered from heavy sintering. In 80wt%Fe_2O_3-CeO_2 the increase was only twofold, which could be due to CeO_2 nanocrystallites acting as a physical barrier and thereby controlling the sintering of iron oxides. The increase of crystallite size was more predominant in 10wt%Fe_2O_3-CeO_2, where sintering yielded a tenfold increase of the iron oxide crystallite size.

Table 1: Crystallite sizes and CeO_2 lattice parameters of as prepared and cycled materials from XRD.

Phase	**10wt%Fe_2O_3-CeO_2**		**80wt%Fe_2O_3-CeO_2**	
	Fresh (nm)	**100 cycles (nm)**	**Fresh (nm)**	**100 cycles (nm)**
CeO_2	15±3	38±4	9±3	35±4
$CeFeO_3$	[b]	75±10	[b]	[b]
Fe_2O_3/Fe_3O_4	5[a,b]	48±13	54±4	98±6
Lattice parameter from CeO_2 (111)	0.5385 ±0.0005	0.5401 ± 0.0007	0.5389 ± 0.0004	0.5401 ± 0.0005

[a]-determined from TEM, [b]- no diffraction peaks present. Error represents standard deviation calculated from 3 most intense peaks.

3.2.2 TEM

The HAADF-STEM image of the as prepared 80wt%Fe_2O_3-CeO_2 sample (Figure 3a) demonstrates the presence of two kinds of particles. The smaller nanoparticles were identified as CeO_2 based on the EELS mapping (Figure 3b). They decorated the larger crystallites of Fe_2O_3 (~50nm). Strong agglomeration of the nanoparticles during cycling (for 100 cycles) led to a significant change of the particle size (Figure 3c). However, the sintered particles of ceria and iron oxide still demonstrate a similar proportion as in the as prepared situation where smaller ceria nanoparticles decorate the larger iron oxide nanoparticles (Figure 3d). The size of the nanoparticles observed after cycling is in agreement with the size retrieved based on XRD data.

The HAADF-STEM image of the as prepared 10wt%Fe_2O_3-CeO_2 (Figure 4a) demonstrates the nanoparticulate morphology of the sample. Elemental mapping (Figure 4b) shows mainly ceria particles to be present. After cycling, the material remains nanosized (Figure 4c), consisting mainly of ceria nanoparticles (Figure 4d). However, several dispersed iron oxide nanoparticles are observed as well. The crystallite sizes calculated from TEM were in agreement with XRD from Table 1.

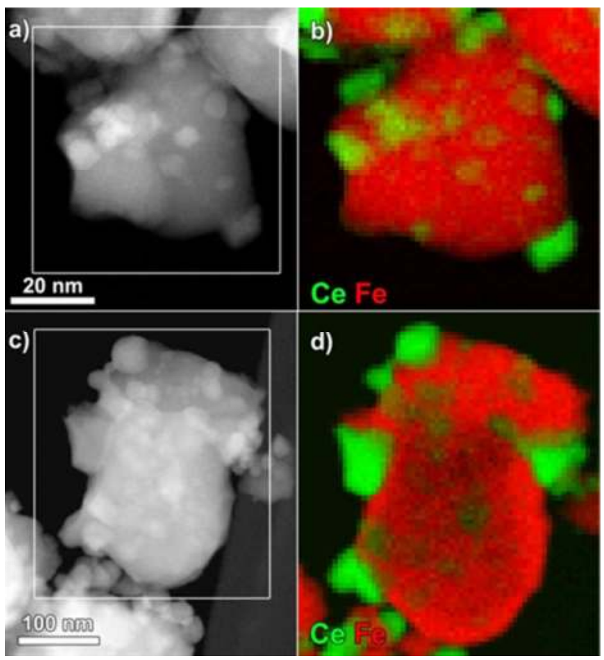

Figure 3: a) HAADF-STEM image of the as prepared 80wt%Fe_2O_3-CeO_2 sample; b) corresponding EELS map for Fe and Ce; c) HAADF-STEM image of the 100 times cycled 80wt%Fe_2O_3-CeO_2 sample; d) corresponding EELS map for Fe and Ce.

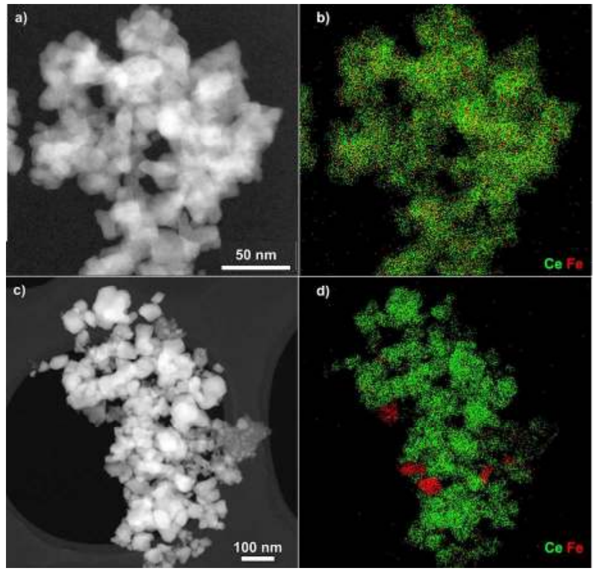

Figure 4: a) HAADF-STEM overview of as prepared 10wt%Fe_2O_3-CeO_2 with b) corresponding EDX map for Ce and Fe. c) HAADF-STEM overview of the 100 times cycled 10wt%Fe_2O_3-CeO_2 sample together with d) corresponding EDX map for Ce and Fe.

3.2.3 XAS: *Structural Modeling*

The incorporation of Fe inside CeO_2 lattice resulted in the formation of solid solution $Ce_{1-x}Fe_xO_{2-x}$ as evidenced from the XRD lattice parameters for CeO_2. The lattice parameter evolution of CeO_2 over a range (2-80wt%Fe_2O_3-CeO_2) of mixed oxide materials (Supplementary Figure S1) shows a plateau between 10wt% and 80wt%Fe_2O_3-CeO_2. This indicates that for each of these materials a similar amount of Fe is incorporated inside the CeO_2 lattice. In addition, in the XRD patterns (Figure 2a (ii)) no major contribution of Fe_2O_3 in 10wt%Fe_2O_3-CeO_2 was present, indicating that a large fraction of Fe can be incorporated inside the CeO_2 lattice. In order to obtain a value for the amount of Fe inside the CeO_2 lattice in as prepared materials, structural modeling was applied to the Ce-K edge EXAFS data. Hence, to determine the amount of Fe dissolved inside the CeO_2 lattice, modeling of 10wt%Fe_2O_3-CeO_2 was pursued at the Ce-K edge. The model was implemented by comparing the CeO_2 fluorite structure and a Fe doped CeO_2

fluorite structure, denoted as $Ce_{1-x}Fe_xO_{2-x}$ where x is the amount of dissolved Fe as parameter to be determined. Both models were fit to the Ce-K EXAFS signal of 10wt%Fe_2O_3-CeO_2 at ambient conditions (Δk = 0.24–1.01 nm^{-1}, ΔR = 0.13–0.41 nm). The fit using the Fe doped CeO_2 structure yielded an *R*-value of 0.0034, whereas for the fit using the pure CeO_2 structure an *R*-value of 0.0064 was obtained. The F test was performed, generating a confidence level α of 94% for the hypothesis that the Fe doped CeO_2 structural model yielded a significantly better fit than the pure CeO_2 model. Consequently, pure CeO_2 was rejected as structural model and thus, the model with Fe doped CeO_2 was chosen as best representing the Fe-doped CeO_2 lattice.

Table 2: Fit results of the Fe incorporated CeO_2 model (Δk = 0.24–1.01 nm^{-1}, ΔR = 0.13–0.41 nm) in R-space with multiple k_i-weighted (i = 1, 2 and 3) to the Ce-K edge EXAFS signal of 10wt%Fe_2O_3-CeO_2 in ambient conditions.

	R (Å)	**N**	**σ^2 (Å^2)**
Ce-O	2.341±0.001	7.61±0.70	0.0078±0.0012
Ce-Ce	3.824±0.002	9.39±2.26	0.0047±0.0016
Ce-Fe	3.843±0.016	2.89±1.20	0.0047±0.0016
Ce-O	4.484±0.002	27±20.12	0.0171±0.0117

The regression fit results of Fe doped CeO_2 are shown in Table 2. The coordination of the first shell remains close to that of pure CeO_2. However, the second shell is split into contributions of Ce and Fe. In order to decorrelate the coordination number N of Fe scatterers in the second shell around the Ce absorber from the Debye–Waller factor for these Fe atoms, the latter was kept equal to the one of the Ce atoms. The Debye–Waller factor of the first Ce-O shell showed a high value, because oxygen as lighter element exhibits a higher entropy. An increase in Debye–Waller factor was also observed in the next O shell due to the light O scatterers and to the Fe incorporation into the lattice of CeO_2. A best fit (Figure 5) was obtained with x = 0.21 ± 0.08 so that 21% of the Ce atoms in CeO_2 is substituted with Fe. This corresponds to 85% of the Fe available, residing within the $Ce_{1-x}Fe_xO_{2-x}$ solid solution in 10wt%Fe_2O_3-CeO_2. For 80wt%Fe_2O_3-CeO_2, it can be assumed that the same amount of Ce is replaced with Fe, i.e. 21mol%, based on the similar CeO_2 lattice parameters. This will of course represent a much smaller fraction of Fe in 80wt%Fe_2O_3-CeO_2 than in 10wt%Fe_2O_3-CeO_2.

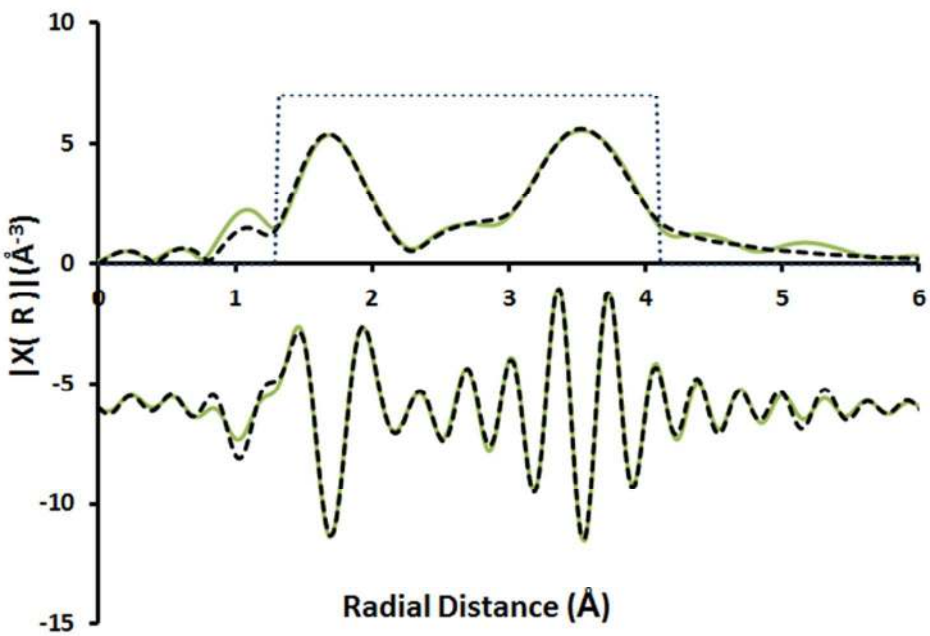

Figure 5: Fourier transformed k^2 -weighted EXAFS signal of 10wt%Fe_2O_3-CeO_2 and k_i -weighted (i = 1, 2 and 3) fit (dashed line) with Fe incorporated CeO_2 model $Ce_{1-x}Fe_xO_{2-x}$ and x = 0.21. The upper part represents the modulus of FT, whereas the lower part is the imaginary part Im[FT{k^2 χ(R)} The dotted rectangle indicates the window fitting range. No phase correction was used. (——) EXAFS signal of 10wt%Fe_2O_3-CeO_2, (- - - -) fit and (·········) fitting window.

3.2.4 In situ characterization: Solid-solid transformation

The material transformations affecting the redox properties during prolonged cycling were investigated during H_2-TPR and CO_2-TPO using in situ XRD[36-39] and conventional temperature-programmed reaction. The crystallographic changes observed in in situ XRD were correlated with the consumption profiles from the conventional temperature-programmed experiments.

3.2.4.1 H_2-TPR

3.2.4.1a 80wt %Fe_2O_3-CeO_2

Figure 6a represents the crystallographic changes during H_2-TPR of as prepared 80wt%Fe_2O_3-CeO_2. The transition of Fe_2O_3 to Fe_3O_4 occurs at a temperature of ~450^{o}C and further transformation of Fe_3O_4 to FeO starts around ~500^{o}C. The deeper reduction of FeO to Fe is identified by the appearance of the diffraction peak of metallic Fe at 2θ=45^o at higher temperature ~600^{o}C. Diffraction peaks for CeO_2 (111) and (200) at 2θ=28^o and 33^o were observed without an apparent phase transformation to Ce_2O_3. This is in agreement with the bulk reduction from CeO_2 to Ce_2O_3 occuring at a much higher temperature[40]. After redox cycling of this material, Fe_3O_4 and CeO_2 are the major phases detected by in situ XRD (Figure 6b). A H_2-TPR of the cycled material shows a faint transition from Fe_3O_4 to FeO at ~500^{o}C, temperature at which also the deeper reduction to metallic Fe starts. The temperature, at which successive reductions occur for both states of the 80wt%Fe_2O_3-CeO_2 sample, was further evaluated based on the diffraction intensity variations segregated from the in situ XRD map (Figure 6c). All phase transitions occur at similar temperature for the as prepared and cycled material.

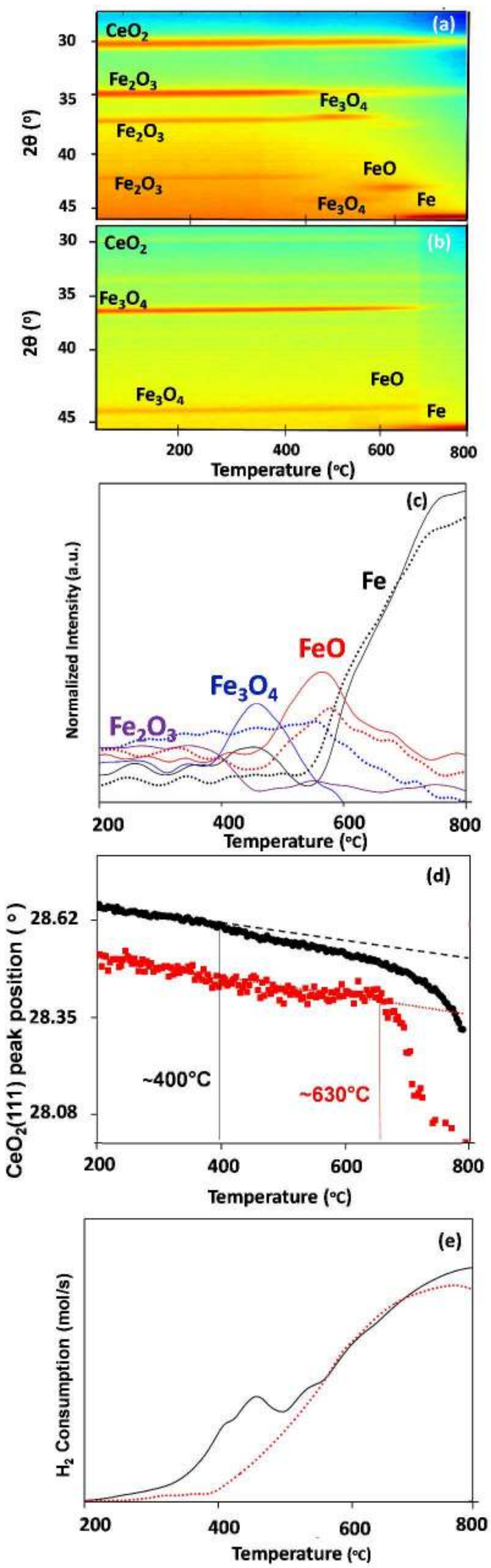

Figure 6: Evolution of 80wt%Fe_2O_3-CeO_2 during H_2-TPR as followed by in situ XRD and conventional TPR. Crystallographic changes of 80wt%Fe_2O_3-CeO_2 in (a) as prepared and (b) 100 times cycled sample; (c) intensity variation of iron oxide phases from in situ XRD in (a) and (b); Intensity changes during in situ XRD of (____) as prepared, (......) 100 times cycled sample; (d) changes in CeO_2 (111) position of as prepared and 100 cycled material; Variation of CeO_2 (111) peak position with temperature for (●) as prepared and (■) 100 times cycled sample; dotted and dashed lines represent thermal lattice expansion; (e) H_2 comsumption profiles during conventional -TPR of (____) as prepared, (......) 100 times cycled sample.

Parallel to iron oxide reduction, CeO_2 could also take part in the reduction, even if no true phase transition takes place. This was verified by following the CeO_2 (111) peak position as a function of temperature (Figure 6d). Thermal lattice expansion induces a gradual lowering of the peak position, indicated by the dashed lines. However, deviations from the extrapolated thermal expansion occur at 400°C for as prepared material, indicating a stronger increase of the lattice size. This is due to partial reduction of the lattice, since Ce^{3+} is larger than Ce^{4+}, which causes an abrupt shift to lower 2θ values at this temperature. For the cycled material, no downward deviation was observed. As indicated by the lattice parameters from XRD (Table 1), the cycling already segregates Fe from the solid solution, which could make the remaining phase less prone to partial reduction. Above 700°C, bulk reduction of CeO_2 sets in, accompanied by a further lattice expansion.

Based on the analysis of in situ XRD, the conventional H_2-TPR profiles can be interpreted in terms of reduction of iron and cerium oxide phases. In Figure 6e a sharp consumption peak at ~450°C is observed for the as prepared material followed by a broad peak around 700°C. Based on in situ XRD (Figure 6a), the consumption peak at ~450°C refers to the transition of Fe_2O_3 to Fe_3O_4 together with the partial reduction of CeO_2 (Figure 6d), which contributes to the onset of the conventional reduction profile. Further reduction from Fe_3O_4 to FeO and FeO to Fe are established within the high temperature single broad peak, together with the start of bulk CeO_2 reduction above 700°C. For the 100 times cycled sample, the single broad peak in the reduction profile corresponds to the simultaneous reduction of Fe_3O_4 to FeO, of FeO to metallic Fe (Figure 6c) and the onset of CeO_2 bulk reduction above 650°C (Figure 6d).

Overall, the complete reduction of Fe_3O_4 to Fe occurs at a relatively higher temperature for the cycled sample than for the as prepared one, due to increased particle size (Table 1). For the partial reduction of CeO_2, the opposite was true. The latter can be understood since cycling results in partial Fe segregation, as evidenced from the increased CeO_2 lattice parameter (Table 1), leading to decreased redox properties.

3.2.4.1b 10wt %Fe_2O_3-CeO_2

A similar in situ XRD analysis was performed on 10wt%Fe_2O_3-CeO_2 to examine the change in reducibility of the as prepared and cycled material. While diffraction peaks of Fe_2O_3 were not observed during the in situ XRD of as prepared material (Figure 7a), metallic Fe appeared above ~600°C. For the cycled material, the phases of CeO_2, perovskite ($CeFeO_3$) and Fe_3O_4 were identified in the sample at the start of TPR (Figure 7b). Reduction to metallic Fe started at a temperature of ~550°C. The diffraction peaks of perovskite ($CeFeO_3$) and CeO_2 remain visible throughout reduction and no peaks corresponding to Ce_2O_3 were observed.

The transition temperature to Fe in as prepared and cycled materials was further evaluated using the integrated diffraction intensities. The intensity plot versus temperature (Figure 7c) shows the onset of formation of metallic Fe in the as prepared sample already starting at ~400°C. For the cycled sample, the formation of metallic Fe is observed around 600°C when Fe_3O_4 is almost completely consumed (Figure 7c). The late onset of reduction of Fe is the result of sintering which leads to an increased crystallite size (Table 1). The latter results in higher reduction temperatures due to a prolonged diffusion time of oxygen from bulk to surface. The reduction to metallic Fe in the cycled sample shifts upward by 200°C, unlike in 80wt%Fe_2O_3-CeO_2 where the reduction to metallic Fe was observed at a similar temperature in the cycled sample. As cycling leads to sintering as evidenced by the crystallite size increase (Table 1) and to formation of perovskite ($CeFeO_3$), these phenomena must be held responsible for the higher reduction temperature of cycled 10wt%Fe_2O_3-CeO_2.

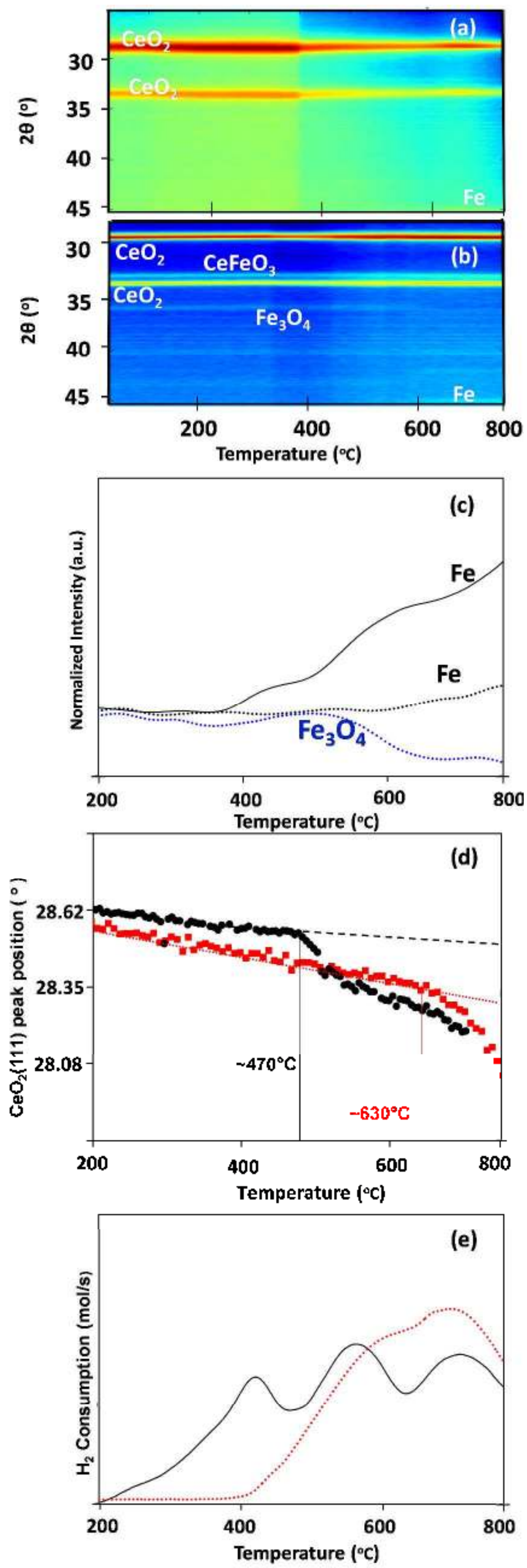

Figure 7: Evolution of 10wt%Fe_2O_3-CeO_2 during H_2-TPR as followed by in situ XRD and conventional TPR: crystallographic changes of (a) as prepared and (b) 100 times cycled sample; Variations of iron oxide diffractions during in situ XRD of (——) as prepared, (……) 100 times cycled sample; (c) intensity variation of iron oxide phases from in situ XRD; (d) changes in CeO_2 (111) position of as prepared and cycled material; Changes of CeO_2 (111) peak position with temperature for (●) as prepared and (■) 100 times cycled sample; dotted and dashed lines represent thermal lattice expansion; (e) H_2 consumption profiles during H_2 (——) as prepared, (……) 100 times cycled material.

Possible reduction of CeO_2 was accessed as before from a peak position analysis (Figure 7d). In as prepared material partial reduction of CeO_2 is seen at ~450°C, while in the cycled sample it hardly occurred before bulk reduction started. The early reduction in the as prepared materials is ascribed to the enhanced reducibility of CeO_2 species promoted by incorporated Fe.

Using the above results from in situ XRD, the conventional H_2-TPR on as prepared and cycled 10wt%Fe_2O_3-CeO_2 were interpreted. The consumption profile for as prepared material shows three peaks (Figure 7e). The first peak at ~425°C can be ascribed to reduction of Fe_2O_3 to Fe_3O_4 as also seen in 80wt%Fe_2O_3-CeO_2, although this transition remained invisible in in situ XRD. The second peak ~550°C could correspond to the early reduction of the Ce^{+4} species promoted by Fe and first reduction to metallic Fe. The third peak follows from reduction to metallic Fe and bulk CeO_2 reduction. For the cycled sample, a single broad H_2 consumption peak is observed arising from the onset of bulk CeO_2 reduction, with a shoulder on the rising edge, originating from iron oxide reduction to metallic Fe.

3.2.4.2 CO_2-TPO

The in situ H_2-TPR was followed by CO_2-reoxidation for all samples. The reoxidation temperatures for partially reduced CeO_2 were evaluated as before from the CeO_2 (111) peak position, and compared with conventional TPO temperatures (Figure 8). The profile of reoxidation for as prepared 10wt%Fe_2O_3-CeO_2 material after reduction (Figure 8a) first peaked at 400°C with the bulk reoxidation occurring at 500°C, whereas that of the 100 times cycled sample appeared in a single peak at 600°C. The CO_2 consumption peak of as prepared material at 400°C corresponds to reoxidation of the solid solution $Ce_{1-x}Fe_xO_{2-x}$, based on the CeO_2 (111) peak position change from in situ XRD (Figure 8b). The second peak corresponds to reoxidation of metallic Fe to Fe_3O_4, which starts at 500°C (Supplementary info Figure S2a) and further reoxidation of Ce^{+3}. For the 100 times cycled sample, the single broad consumption curve represents the combined reoxidation of Ce^{+3} above 450°C and metallic Fe from 550°C on (Figure 8b and supplementary info Figure S2b).

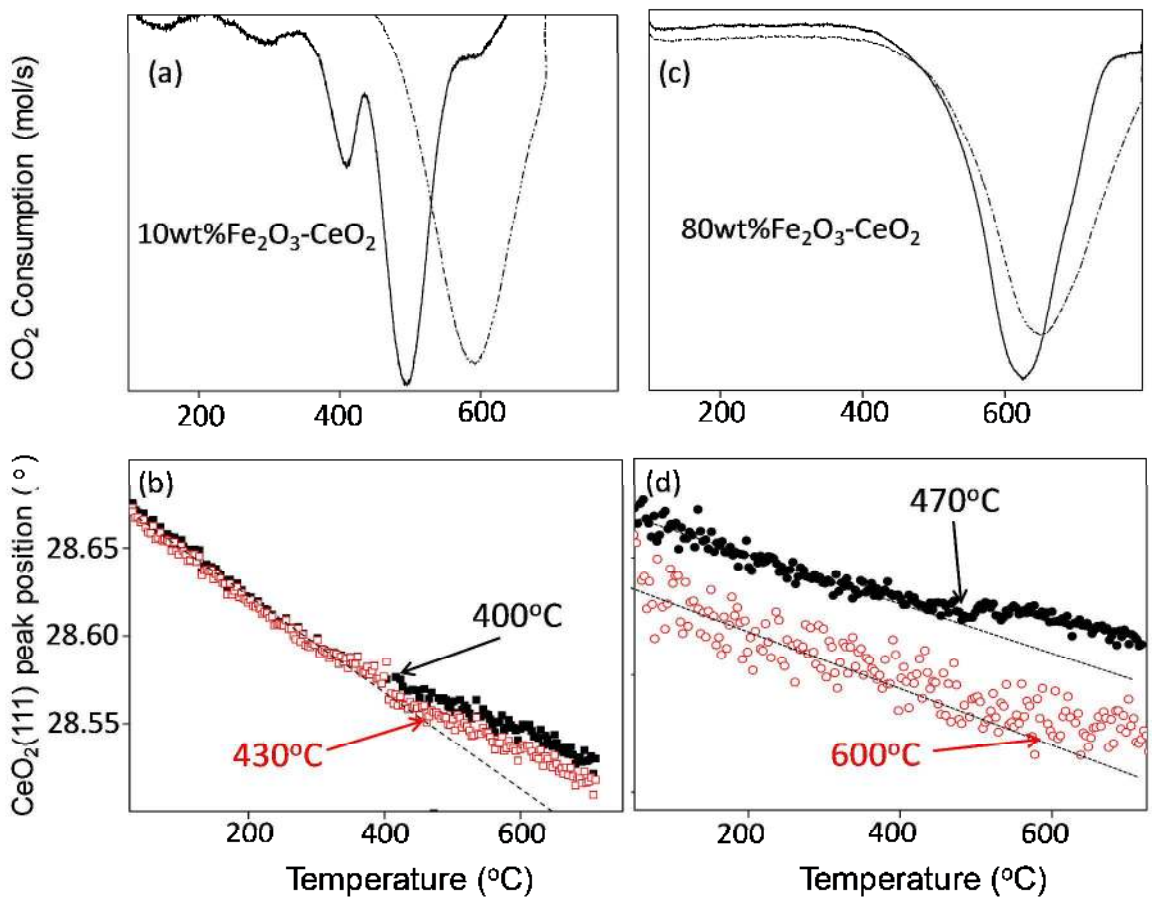

Figure 8: conventional reoxidation profiles of (a) 10wt%Fe_2O_3-CeO_2 and (c) 80wt% Fe_2O_3-CeO_2, as prepared and 100 cycled; changes in the CeO_2 (111) peak position during CO_2 reoxidation of (b) 10wt%Fe_2O_3-CeO_2 and (d) 80wt% Fe_2O_3-CeO_2, as prepared and 100 times cycled. Comsumption profiles during conventional CO_2-TPO of (——) As prepared, (– · · –) 100 times cycled sample. CeO_2 peak position of 10wt%Fe_2O_3-CeO_2 (■) as prepared, (□) 100 times cycled and 80wt%Fe_2O_3-CeO_2 (●) as prepared and (○) 100 times cycled sample. Each cycle (16 min) is composed of 4 min H_2 (5% in Ar), 4 min He, 4 min CO_2 (100%) and 4 min He at 650°C. All the gas flows were 1.1 Nml/s.

A similar analysis was performed for 80wt%Fe_2O_3-CeO_2. The reoxidation of as prepared and cycled materials of 80wt%Fe_2O_3-CeO_2 (Figure 8c) peaked at similar temperatures (~600°C). The position analysis of CeO_2(111) shows that partial reoxidation of Ce^{+3} to Ce^{+4} occurs at ~470°C for as prepared material and at ~600°C for the 100 times cycled sample (Figure 8d). These temperatures fall within the conventional reoxidation profile of both materials. In addition, these broad peaks contain a contribution from the reoxidation of metallic Fe to Fe_3O_4, occurring at 400°C for as prepared and at 350°C for cycled material (Supplementary info Figure S3a&b). Similar reoxidation temperatures were observed in the fresh and cycled samples for 80wt%Fe_2O_3-CeO_2, whereas in 10wt%Fe_2O_3-CeO_2 the reoxidation of the cycled sample shifted to higher temperatures.

4.0 Discussion

In chemical looping, deactivation of Fe_2O_3-CeO_2 oxygen storage materials is observed as a decline in CO yield as a function of redox cycles. Extensive characterization of materials, by means of In situ XRD, TEM and XAS, showed the latter is due to a combination of solid-solid transformation and sintering. The former comprises the formation of a new phase and/or elemental segregation. Sintering on the other hand leads to an increase of crystallite size and, hence, smaller surface area. The nature and extent of these changes determine the overall yield of the chemical looping reaction in a prolonged redox process.

4.1 Solid-solid transformation

The first kind of deactivation is due to strong promoter and support interaction during prolonged redox cycling. For the materials of the present study, solid-solid transformation can be categorized into two types: 1) formation of a perovskite phase $CeFeO_3$ due to interaction of Fe and CeO_2 during redox cycling[41-44] and 2) segregation of Fe from the solid solution $Ce_{1-x}Fe_xO_{2-x}$[23]. The perovskite formation was identified using in situ XRD and XAS, while the segregation of Fe was identified using the XRD lattice parameter evolution during the first 10 cycles.

In the first type of deactivation, the amount of exchangeable oxygen is restricted by the nature of the phase formed. If the new phase remains inert to reduction and oxidation, this results in a decrease of oxygen available for reaction and hence lowering of the oxygen storage capacity. The second type of deactivation, segregation of Fe from $Ce_{1-x}Fe_xO_{2-x}$ leads to destruction of the solid solution and higher reduction temperatures for CeO_2, which is not beneficial for the redox process[16, 54, 55].

4.1.1 Perovskite formation ($CeFeO_3$)

To assess the influence of $CeFeO_3$ on the redox properties during cycling, pretreated 50wt%Fe_2O_3-CeO_2 was investigated using in situ XRD. The peak position analysis of $CeFeO_3$ (112) during H_2-TPR and CO_2-TPO (Supplementary info Figure S4) showed a steady shift towards lower two theta values, due to thermal lattice expansion. Hence, the perovskite phase didn't show reducibility in the given temperature range, and the formation of $CeFeO_3$ only led to loss of active metal available for reaction.

4.1.2 Segregation of Fe

For as prepared materials, Ce-K EXAFS modelling revealed around 21mol% of Ce substituted by Fe inside $Ce_{1-x}Fe_xO_{2-x}$. TEM images show the presence of atomically dispersed Fe throughout CeO_2, while the CeO_2 lattice parameter calculations from XRD indicate that an amount of Fe was incorporated inside the lattice of CeO_2 (Supplementary info Figure S1).

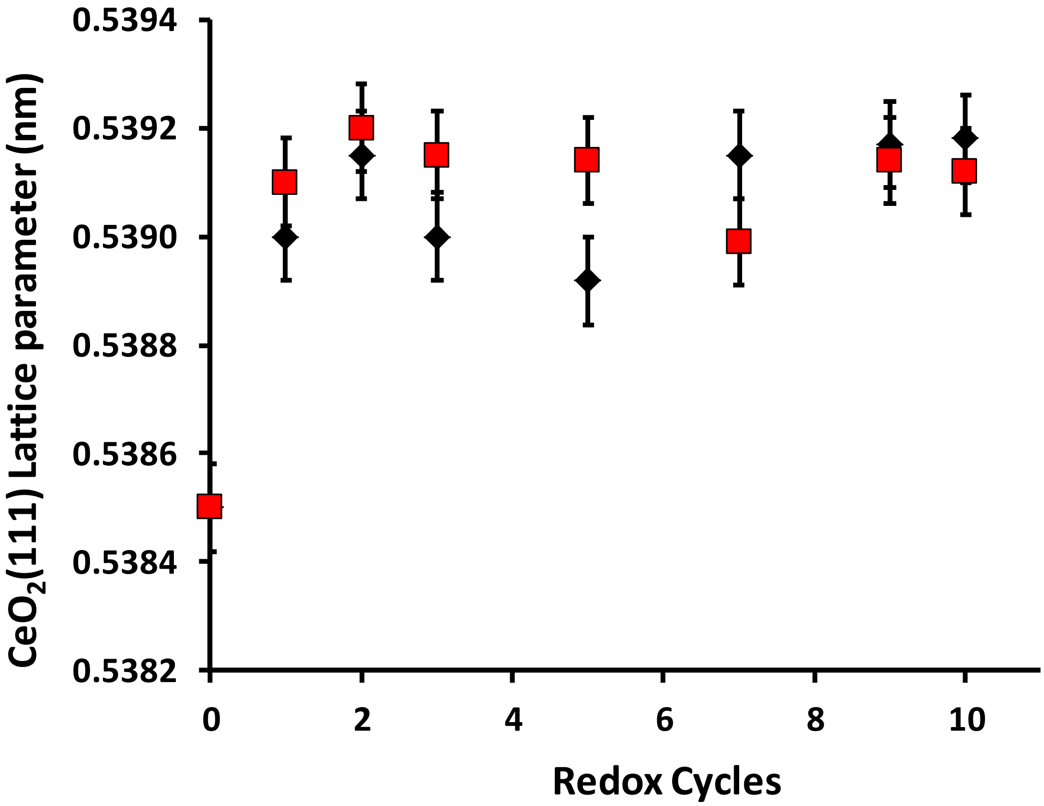

Figure 9: The CeO_2 lattice parameters of cycled 10wt% Fe_2O_3-CeO_2 and 80wt%Fe_2O_3-CeO_2 as a function of cycles Lattice parameters of (■) 80wt%Fe_2O_3-CeO_2 and (◆) 10wt%Fe_2O_3-CeO_2. The error bars represent standard error (68% confidence interval) calculated from 3 most intense peaks.

In previous work on 5wt%Fe_2O_3-CeO_2, agglomeration of segregated Fe was observed in TEM after 10 redox cycles, leading to nanoclusters at the CeO_2 grain boundaries[23]. To further investigate the phenomenon of Fe segregation, lattice parameter calculations were performed after each redox cycle (Figure 9). It turned out that Fe was segregated from the CeO_2 lattice upon the very first redox cycle, while for subsequent cycles, the lattice parameter levelled off between 0.5389-0.5392nm. When comparing these values to those after 100 cycles (Table 1), it appears that the unit cell parameters do increase further, from 0.5389-0.5392nm at cycle 10 (Figure 9) to

0.5401nm upon cycle 100 (Table 1). This indicates that an amount of Fe is segregated easily in the first redox cycle, but further withdrawal of Fe proceeds much slower.

The effect of Fe segregation upon the redox properties of the material can be twofold. On the one hand, it destroys the solid solution $Ce_{1-x}Fe_xO_{2-x}$, which in turn will lead to more elevated redox temperatures and enhanced sintering for CeO_2. On the other hand, the segregated Fe can contribute to the redox capacity of iron oxides, but is also likely to suffer from sintering.

4.2 Sintering

During sintering the overall oxygen available remains unchanged, but the increased diffusion time of oxygen from the bulk to the surface leads to a loss of CO yield. To assess when the effect of sintering sets in, the change in crystallite size of both CeO_2 and Fe_3O_4 was determined as a function of cycles (Figure 10). Sintering of iron oxide is more rapid in 10wt%Fe_2O_3-CeO_2 than in 80wt%Fe_2O_3-CeO_2 (Figure 10). For 10wt%Fe_2O_3-CeO_2, the increase in crystallite size of iron oxide is especially steep after the first cycle: from 5nm Fe_2O_3 particles in as prepared material to ~30nm Fe_3O_4 after 1 redox cycle. This huge size increase will relate not only to sintering of the Fe_2O_3 nanoparticles originally present, but also to Fe segregated from CeO_2, as an important fraction of Fe is segregated from $Ce_{1-x}Fe_xO_{2-x}$ after the first cycle (Figure 9). For further redox cycles, crystal growth continues but after cycle 10, the size is already close to the value after 100 cycles (Table 1). In parallel to Fe_3O_4 particle size growth, also CeO_2 sinters, possibly more rapidly as the solid solution between Ce and Fe deteriorates.

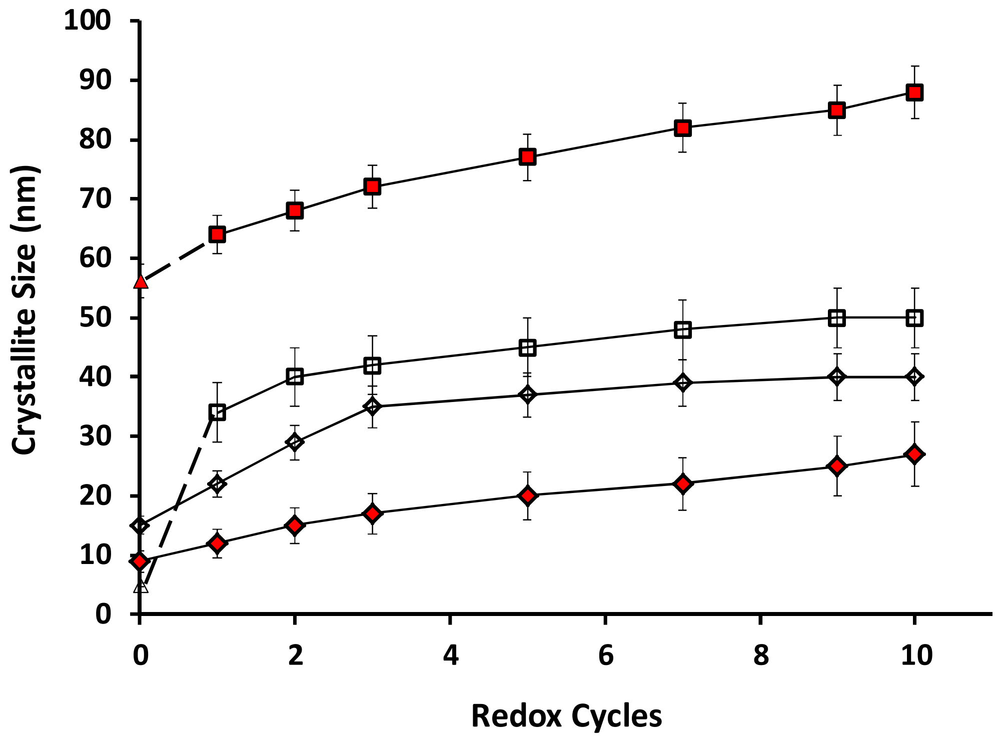

Figure 10: Crystallite sizes of CeO_2 and Fe_3O_4 during the first 10 redox cycles of 10wt%Fe_2O_3-CeO_2 and 80wt%Fe_2O_3-CeO_2. (△) Fe_2O_3 in as prepared material, (□) Fe_3O_4 and (◇) CeO_2 crystallite sizes in 10wt%Fe_2O_3-CeO_2. (▲) Fe_2O_3 in as prepared material, (■) Fe_3O_4 and (◆) CeO_2 crystallite sizes in 80wt%Fe_2O_3-CeO_2 (- - - - -) guide for crystallite size evolution from Fe_2O_3 to Fe_3O_4, (——) guide to the eye for crystallite size increase between similar phase. Error bars represent standard deviation (68% confidence interval) calculated from 3 most intense peaks.

In 80wt%Fe_2O_3-CeO_2, large particles of Fe_2O_3 are present from the start with $Ce_{1-x}Fe_xO_{2-x}$ as physical barrier in between them. Sintering of Fe_3O_4 in the first 10 cycles is less severe than in 10wt%Fe_2O_3-CeO_2. From the value after 100 cycles (Table 1) it follows that particle size will keep increasing throughout cycling operation. However, compared to pure iron oxide the loss in CO yield is significantly reduced[24]. For the solid solution $Ce_{1-x}Fe_xO_{2-x}$, particle sizes increase mostly in the first 10 cycles, i.e. when Fe is segregated from the lattice, but remain relatively stable afterwards (Table 1).

4.3 Deactivation of 10wt%Fe_2O_3-CeO_2 and 80wt% Fe_2O_3-CeO_2

Different forms of deactivation have been identified in 10wt%Fe_2O_3-CeO_2 and 80wt% Fe_2O_3-CeO_2: solid-solid transformation to perovskite ($CeFeO_3$), segregation of Fe, and sintering, each playing a role in the loss of CO yield. The way in which each mechanism of deactivation affects the materials largely depends on their bulk composition. In 10wt%Fe_2O_3-CeO_2, CeO_2 is the bulk oxygen storage carrier, while in 80wt% Fe_2O_3-CeO_2 it is Fe_2O_3 and these will largely determine the behaviour of the oxygen storage material in a chemical looping process.

In 10wt%Fe_2O_3-CeO_2, iron oxide promotes the active material by enhancing the redox properties of CeO_2. The latter is achieved by the dissolution of Fe into the lattice of CeO_2, thereby creating vacancies that facilitate the oxygen mobility and allow easy diffusion of oxygen from the bulk. The resulting solid solution $Ce_{1-x}Fe_xO_{2-x}$ is known for its enhanced redox properties. Upon prolonged cycling of 10wt%Fe_2O_3-CeO_2, deactivation occurs due to sintering, perovskite formation and segregation of Fe from $Ce_{1-x}Fe_xO_{2-x}$. In a redox atmosphere, Fe segregates out of the lattice of CeO_2 and sinters rapidly along with CeO_2, in parallel to the perovskite phase transformation. This results in loss of reducibility as observed in TPR and TPO of the cycled material (Figure 7e and 8a). The deactivation in 10wt%Fe_2O_3-CeO_2 materials is summarized in Figure 11a.

In 80wt%Fe_2O_3-CeO_2, Fe_3O_4 is the bulk oxygen carrier and CeO_2 acts as chemically active promoter. In as prepared material, $Ce_{1-x}Fe_xO_{2-x}$ solid solution particles decorate the larger iron oxide crystallites (Figure 3). After cycling, all particle sizes have increased but the overall structure of decoration remains unchanged. A distinct perovskite phase is not observed, but cannot be excluded. Overall, the reducibility of this sample is largely preserved after cycling (Figure 6e and 8c). The role of the decorating CeO_2 crystallites is mainly preventing physical contact of iron oxide with only limited contribution to the oxygen storage capacity. The behavior of 80wt%Fe_2O_3-CeO_2 can be represented as in Figure 11b.

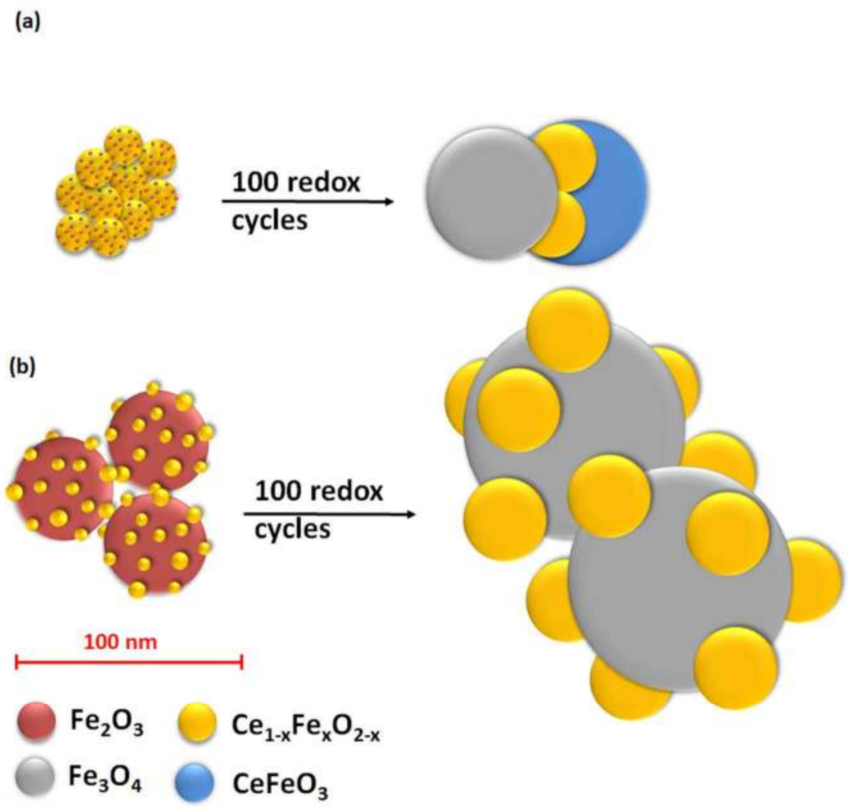

Figure 11: Deactivation in (a) 10wt%Fe_2O_3-CeO_2 and (b) 80wt%Fe_2O_3-CeO_2 after 100 redox cycles.

4.4 Material deactivation: what to do?

To counter the observed types of deactivation, several options are available. The formation of a perovskite phase in 10wt%Fe_2O_3-CeO_2 or similar CeO_2-rich materials can be avoided by applying a regeneration process. In contrast to CO_2-TPO, O_2-TPO is capable to decompose perovskite and restore the redox phases The material is decomposed into CeO_2 and Fe_2O_3

around 400°C. Figure 12 confirms that for both materials, an O_2 treatment is beneficial to the CO yield. An increase is observed in 10wt%Fe_2O_3-CeO_2 (Figure 12). In this material, a significant perovskite phase is present after cycling, as evidenced by XRD (Figure 2b(ii)). Similar to pre-treated 50wt%Fe_2O_3-CeO_2, the O_2 treatment likely decomposes the perovskite ($CeFeO_3$) structure and leads to the regeneration of the oxygen carriers Fe_2O_3 and CeO_2, with corresponding restoring of the CO yield. However, the regeneration does not bring back the original CO yield and moreover, it is lost very rapidly when cycling is continued. Hence, loss of oxygen storage capacity due to perovskite formation is an important deactivation pathway in this sample.

In 80wt%Fe_2O_3-CeO_2 hardly any increase in the CO yield upon O_2 treatment was observed. This could be related to the fact that the perovskite ($CeFeO_3$) being less present after cycling this material (Figure 2b(i)). Unlike in 10wt%Fe_2O_3-CeO_2, perovskite formation is not the cause of CO yield degeneration in 80wt%Fe_2O_3-CeO_2, which will mainly proceed through other forms of deactivation.

The effect of deactivation due to sintering appears from the regeneration study of the samples (Figures 12 and Figure 1). Despite the restoration of Fe_2O_3 and CeO_2 phases by means of O_2 treatment, the materials could not regain the CO yield of the as prepared materials because of the increased crystallite size. For Fe_2O_3-rich materials, sintering is the dominant process to be countered.

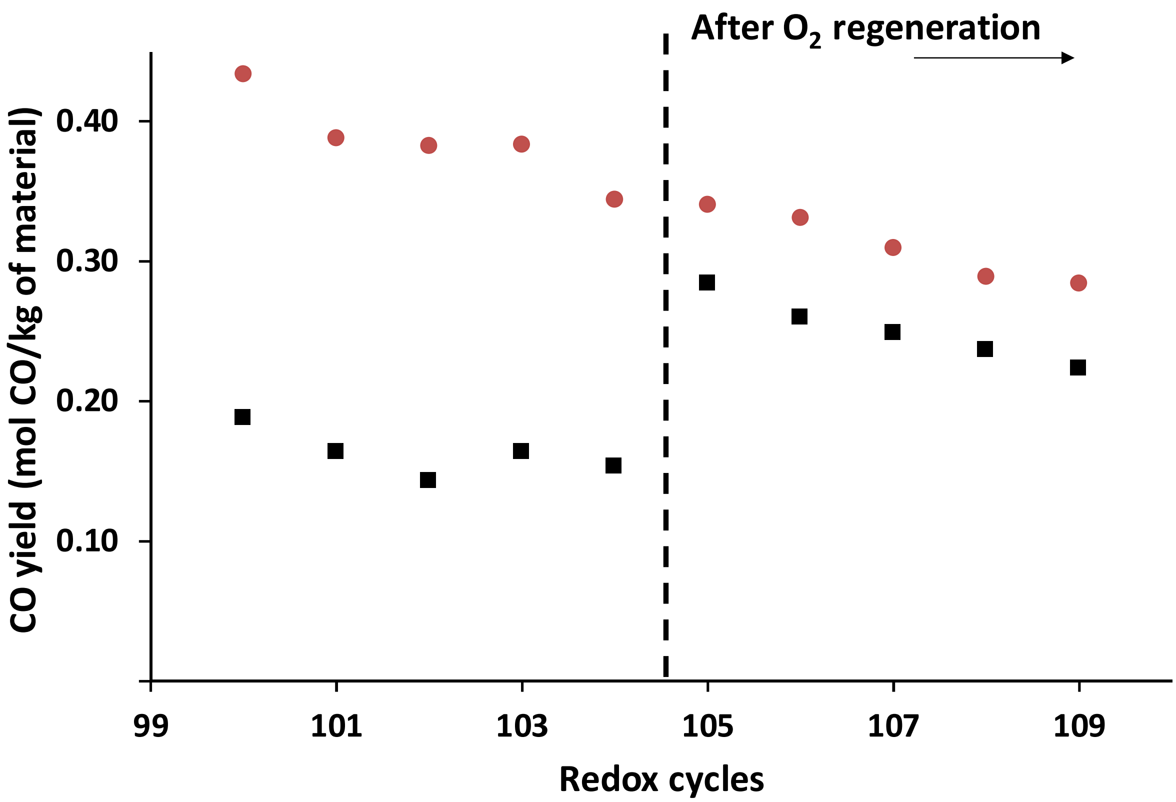

Figure 12: Regeneration study of 10wt%Fe_2O_3-CeO_2 and 80wt%Fe_2O_3-CeO_2 by means of O_2 treatment. (■) 10wt%Fe_2O_3-CeO_2 and (●) 80wt%Fe_2O_3-CeO_2.

Sintering is physical process which leads to the loss of material surface due to crystallite growth of either the support material or the active phase. Sintering is strongly temperature dependent. The core mechanism is surface diffusion, or, at sufficiently high temperature, mobility of larger aggregates. This leads to a correlation with the melting point. The solid-state diffusion becomes faster when the temperature is closer to the melting point. The so-called Hüttig and Tamman temperatures are indicative for the temperature at which sintering may occur. When the Hüttig temperature is reached, atoms at defects will become mobile. At the Tamman temperature, atoms from the bulk will show mobility, while at the melting temperature, overall mobility will be really high. The following empirical relations for the Hüttig and Tamman temperatures are recommended for use:

$$T_{\text{Hüttig}} = 0.3T_{\text{melting}}$$

$$T_{\text{Tamman}} = 0.5T_{\text{melting}}$$

In the reducing and oxidizing atmosphere of a chemical looping process, the thermal stability of the material changes depending on the material state. For example, the melting temperatures for Fe_2O_3, Fe_3O_4, FeO and Fe are 1565°C, 1597°C, 1377°C and 1538°C respectively. The formation of FeO during the reduction/oxidation process will naturally decrease the material melting temperature, which can lead to fast material sintering. Sintering is best avoided by minimizing and controlling the temperature of reaction, although recent developments have focused on encapsulating metal crystallites to eliminate mobility, while still allowing access for reactants and products.

The decoration of Fe_2O_3 with small CeO_2 crystallites provides a valid strategy for reduced sintering but could be improved. Various promoter materials can be used for this approach, but most of them give rise to solid-solid transformation leading to lower CO production. The properties of CeO_2 can be further enhanced by adding a second element, e.g. ZrO_2, $CeZrO_2$. Those materials presents high resistance to sintering and in addition, will not form a perovskite phase with iron oxide.

5.0 Conclusions

10wt%Fe_2O_3-CeO_2 and 80wt%Fe_2O_3-CeO_2 oxygen storage materials were subjected to prolonged redox cycling to study their deactivation. Three types of deactivation were identified: sintering, Fe segregation from solid solution and perovskite formation, leading to a loss of CO yield. The segregation of Fe from the $Ce_{1-x}Fe_xO_{2-x}$ occurs very fast, from the first redox cycle on. It leads to lower reducibility of CeO_2, but at the same time provides more iron oxide storage capacity after decomposition of perovskite ($CeFeO_3$) resulting in more reducible Fe. Perovskite ($CeFeO_3$) forms in the first tens of cycles and leads to a loss of oxygen storage capacity as it is non-reducible. Sintering then again is a slower process which continues throughout cyclic operation. It causes crystallites to grow in size, thereby increasing the diffusion time of bulk oxygen to the surface. Hence, a lower degree of reduction is reached and upon reoxidation a lower CO yield is obtained.

The relative importance of these deactivation types depends on the composition of the oxygen storage material. In 80wt%Fe_2O_3-CeO_2 deactivation is predominantly caused by sintering of iron oxides. Fe segregation is of minor importance given the composition of this material. Similarly, perovskite formation may possibly occur, but will hardly affect the cycling productivity. In 10wt%Fe_2O_3-CeO_2 all three types of deactivation are at play, this is why deactivation for this composition is more rapid and severe during the first 10 cycles.

A regeneration study shows that after treatment with O_2, the CO yield for both materials increases slightly. The increase in the CO yield is more prominent in 10wt%Fe_2O_3-CeO_2, where the O_2 treatment leads to decomposition and phase segregation of $CeFeO_3$. However, the overall CO yield remains lower than at the start of cycling, showing the importance of sintering in this material.

In terms of CO yield, 80wt%Fe_2O_3-CeO_2 stands out as the best material for prolonged cycling. In this material, the main deactivation type sintering is reduced by the strategy of decorating Fe_2O_3 with CeO_2 nanoparticles. Based on this deactivation study, replacing CeO_2 with a compound that does not undergo solid-solid transformations, could prove worthwhile in view of further countering deactivation.

Acknowledgements

This work was supported by the Long Term Structural Methusalem Funding by the Flemish Government, the Fund for Scientific Research Flanders (FWO; project G004613N) and The Interuniversity Attraction Poles Programme, IAP7/5 Belgian State – Belgian Science Policy (BELSPO). The authors acknowledge the Fund for Scientific Research Flanders (FWO-Vlaanderen) in supplying financing of beam time at the DUBBLE and SNBL beam line of the ESRF and travel costs. The authors also thank the assistance of the DUBBLE and SNBL staff and equally acknowledge the technical support from Geert Rampelberg with the in situ XRD equipment (Department of Solid State Sciences, Ghent University).

Supporting Information

Lattice parameter evolution (Figure S1), in situ XRD during CO_2-TPO of 10wt%Fe_2O_3-CeO_2 (Figure S2a&b), in situ XRD during CO_2-TPO of 80wt%Fe_2O_3-CeO_2 (Figure S3a&b), $CeFeO_3$ peak position (Figure S4).

References

1. Chueh, W. C.; Falter, C.; Abbott, M.; Scipio, D.; Furler, P.; Haile, S. M.; Steinfeld, A., High-Flux Solar-Driven Thermochemical Dissociation of CO_2 and H_2O Using Nonstoichiometric Ceria. Science 2010, 330, 1797-1801.
2. Du, N.; Park, H. B.; Robertson, G. P.; Dal-Cin, M. M.; Visser, T.; Scoles, L.; Guiver, M. D., Polymer nanosieve membranes for CO_2-capture applications. Nat. Mater. 2011, 10, 372-375.
3. Yang, H.; Xu, Z.; Fan, M.; Gupta, R.; Slimane, R. B.; Bland, A. E.; Wright, I., Progress in carbon dioxide separation and capture: A review. J. Environ. Sci. 2008, 20, 14-27.
4. Sheps, K. M.; Max, M. D.; Osegovic, J. P.; Tatro, S. R.; Brazel, L. A., A case for deep-ocean CO_2 sequestration. Energy Procedia 2009, 1, 4961-4968.
5. Doucet, F. J., Effective CO_2-specific sequestration capacity of steel slags and variability in their leaching behaviour in view of industrial mineral carbonation. Miner. Eng. 2010, 23, 262-269.

6. Shao, H.; Ray, J. R.; Jun, Y.-S., Dissolution and Precipitation of Clay Minerals under Geologic CO_2 Sequestration Conditions: CO_2−Brine−Phlogopite Interactions. Environ. Sci. Technol. 2010, 44, 5999-6005.
7. Zhang, W. E. I., Density-driven enhanced dissolution of injected CO_2 during long-term CO_2 geological storage. J. Earth Syst. Sci. 2013, 122, 1387-1397.
8. Khoo, H. H.; Tan, R. B. H., Environmental impact evaluation of conventional fossil fuel production (oil and natural gas) and enhanced resource recovery with potential CO_2 sequestration. Energy Fuels 2006, 20, 1914-1924.
9. Galvita, V. V.; Poelman, H.; Marin, G. B., Combined chemical looping for energy storage and conversion. J. Power Sources 2015, 286, 362-370.
10. Fan, L. S.; Zeng, L.; Wang, W. L.; Luo, S. W., Chemical looping processes for CO_2 capture and carbonaceous fuel conversion - prospect and opportunity. Energy Environ. Sci. 2012, 5, 7254-7280.
11. Bhavsar, S.; Najera, M.; Veser, G., Chemical Looping Dry Reforming as Novel, Intensified Process for CO_2 Activation. Chem. Eng. Technol. 2012, 35, 1281-1290.
12. Fan, L. S.; Zeng, L.; Luo, S. W., Chemical Looping Rises to the Challenge. Chem. Eng. Prog. 2015, 111, 30-38.
13. Dai, X. P.; Li, J.; Fan, J. T.; Wei, W. S.; Xu, J., Synthesis Gas Generation by Chemical-Looping Reforming in a Circulating Fluidized Bed Reactor Using Perovskite $LaFeO_3$-Based Oxygen Carriers. Ind. Eng. Chem. Res. 2012, 51, 11072-11082.
14. Cabello, A.; Dueso, C.; Garcia-Labiano, F.; Gayan, P.; Abad, A.; de Diego, L. F.; Adanez, J., Performance of a highly reactive impregnated Fe_2O_3/Al_2O_3 oxygen carrier with CH4 and H_2S in a 500 W-th CLC unit. Fuel 2014, 121, 117-125.
15. Galvita, V. V.; Poelman, H.; Detavernier, C.; Marin, G. B, Catalyst-assisted chemical looping for CO_2 conversion to CO. Appl. Catal., B 2015, 164, 184–191.
16. Galvita, V. V.; Poelman, H.; Bliznuk, V.; Detavernier, C.; Marin, G. B., CeO_2-Modified Fe_2O_3 for CO_2 Utilization via Chemical Looping. Ind. Eng. Chem. Res. 2013, 52, 8416-8426.
17. Lyngfelt, A., Oxygen Carriers for Chemical Looping Combustion-4000 h of Operational Experience. Oil Gas Sci. Technol. 2011, 66, 161-172.
18. Bayham, S.; McGiveron, O.; Tong, A.; Chung, E.; Kathe, M.; Wang, D. W.; Zeng, L.; Fan, L. S., Parametric and dynamic studies of an iron-based 25-kW(th) coal direct chemical looping unit using sub-bituminous coal. Appl. Energy 2015, 145, 354-363.
19. A. Tong, S. Bayham, M.V. Kathe, L. Zeng, S. Luo, L.-S. Fan, Iron-based syngas chemical looping process and coal-direct chemical looping process development at Ohio State University, Appl. Energy, 2014, 113, 1836-1845.
20. Galvita, V.; Hempel, T.; Lorenz, H.; Rihko-Struckmann, L. K.; Sundmacher, K., Deactivation of modified iron oxide materials in the cyclic water gas shift process for CO-free hydrogen production. Ind. Eng. Chem. Res. 2008, 47, 303-310.
21. Datta, P.; Rihko-Struckmann, L. K.; Sundmacher, K., Influence of molybdenum on the stability of iron oxide materials for hydrogen production with cyclic water gas shift process. Mater. Chem. Phys. 2011, 129, 1089-1095.
22. Galvita, V. V.; Filez, M.; Poelman, H.; Bliznuk, V.; Marin, G. B., The Role of Different Types of CuO in $CuO-CeO_2/Al_2O_3$ for Total Oxidation. Catal. Lett. 2014, 144, 32-43.

23. Meledina, M.; Turner, S.; Galvita, V. V.; Poelman, H.; Marin, G. B.; Van Tendeloo, G., Local environment of Fe dopants in nanoscale Fe : CeO_{2-x} oxygen storage material. Nanoscale 2015, 7, 3196-3204.
24. Galvita, V.; Sundmacher, K., Redox behavior and reduction mechanism of Fe_2O_3-$CeZrO_2$ as oxygen storage material. J. Mater. Sci. 2007, 42, 9300-9307.
25. Mattisson, T.; Lyngfelt, A.; Cho, P., The use of iron oxide as an oxygen carrier in chemical-looping combustion of methane with inherent separation of CO_2. Fuel 2001, 80, 1953-1962.
26. Kidambi, P. R.; Cleeton, J. P. E.; Scott, S. A.; Dennis, J. S.; Bohn, C. D., Interaction of Iron Oxide with Alumina in a Composite Oxygen Carrier during the Production of Hydrogen by Chemical Looping. Energy Fuels 2012, 26, 603-617.
27. Kierzkowska, A. M.; Bohn, C. D.; Scott, S. A.; Cleeton, J. P.; Dennis, J. S.; Muller, C. R., Development of Iron Oxide Carriers for Chemical Looping Combustion Using Sol-Gel. Ind. Eng. Chem. Res. 2010, 49, 5383-5391.
28. Galvita, V. V.; Poelman, H.; Marin, G. B., Hydrogen Production from Methane and Carbon Dioxide by Catalyst-Assisted Chemical Looping. Top. Catal. 2011, 54, 907-913.
29. Zafar, Q.; Mattisson, T.; Gevert, B., Integrated hydrogen and power production with CO2 capture using chemical-looping reforming-redox reactivity of particles of CuO, Mn2O3, NiO, and Fe_2O_3 using SiO_2 as a support. Ind. Eng. Chem. Res. 2005, 44, 3485-3496.
30. Corbella, B. M.; Palacios, J. M., Titania-supported iron oxide as oxygen carrier for chemical-looping combustion of methane. Fuel 2007, 86, 113-122.
31. Leion, H.; Mattisson, T.; Lyngfelt, A., The use of petroleum coke as fuel in chemical-looping combustion. Fuel 2007, 86, 1947-1958.
32. Shulman, A.; Linderholm, C.; Mattisson, T.; Lyngfelt, A., High Reactivity and Mechanical Durability of $NiO/NiAl_2O_4$ and $NiO/NiAl_2O_4/MgAl_2O_4$ Oxygen Carrier Particles Used for more than 1000 h in a 10 kW CLC Reactor. Ind. Eng. Chem. Res. 2009, 48, 7400-7405.
33. Johansson, M.; Mattisson, T.; Lyngfelt, A., Investigation of Fe_2O_3 with $MgAl_2O_4$ for chemical-looping combustion. Ind. Eng. Chem. Res. 2004, 43, 6978-6987.
34. Dharanipragada, N. V. R. A.; Buelens, L. C.; Poelman, H.; De Grave, E.; Galvita, V. V.; Marin, G. B., Mg-Fe-Al-O for advanced CO_2 to CO conversion: carbon monoxide yield vs. oxygen storage capacity. J. Mater. Chem. A 2015, 3, 16251-16262.
35. Rihko-Struckmann, L. K.; Datta, P.; Wenzel, M.; Sundmacher, K.; Dharanipragada, N. V. R. A.; Poelman, H.; Galvita, V. V.; Marin, G. B., Hydrogen and Carbon Monoxide Production by Chemical Looping over Iron-Aluminium Oxides. Energy Technol. 2015, 3, 1-11.
36. Bobin, A. S.; Sadykov, V. A.; Rogov, V. A.; Mezentseva, N. V.; Alikina, G. M.; Sadovskaya, E. M.; Glazneva, T. S.; Sazonova, N. N.; Smirnova, M. Y.; Veniaminov, S. A.; Mirodatos, C.; Galvita, V.; Marin, G. B., Mechanism of CH4 Dry Reforming on Nanocrystalline Doped Ceria-Zirconia with Supported Pt, Ru, Ni, and Ni–Ru. Top. Catal. 2013, 56, 958-968.
37. Galinsky, N. L.; Shafiefarhood, A.; Chen, Y.; Neal, L.; Li, F., Effect of support on redox stability of iron oxide for chemical looping conversion of methane. Appl. Catal., B 2015, 164, 371-379.
38. Tang, M.; Xu, L.; Fan, M., Progress in oxygen carrier development of methane-based chemical-looping reforming: A review. Appl. Energy 2015, 151, 143-156.
39. Zhu, X.; Li, K.; Wei, Y.; Wang, H.; Sun, L., Chemical-Looping Steam Methane Reforming over a CeO_2–Fe_2O_3 Oxygen Carrier: Evolution of Its Structure and Reducibility. Energy Fuels 2014, 28, 754-760.

40. Ravel, B.; Newville, M., ATHENA and ARTEMIS: Interactive graphical data analysis using IFEFFIT. Phys. Scr. 2005, T115, 1007-1010.
41. Koningsberger, D. C.; Mojet, B. L.; van Dorssen, G. E.; Ramaker, D. E., XAFS spectroscopy; fundamental principles and data analysis. Top. Catal. 2000, 10, 143-155.
42. J.J. Rehr, J.M. Deleon, S.I. Zabinsky, R.C. Albers, Theoretical X-Ray Absorption Fine-Structure Standards, J. Am. Chem. Soc. 1991, 113, 5135-5140.
43. Hamilton, W. C., Significance Tests on Crystallographic R Factor. Acta Crystallogr. A 1965, 18, 502-&.
44. Bacchi, A.; Lamzin, V. S.; Wilson, K. S., A self-validation technique for protein structure refinement: The extended Hamilton test. Acta Crystallogr D 1996, 52, 641-646.
45. Zielinski, J.; Zglinicka, I.; Znak, L.; Kaszkur, Z., Reduction of Fe_2O_3 with hydrogen. Appl. Catal., A 2010, 381, 191-196.
46. Rampelberg, G.; De Schutter, B.; Devulder, W.; Martens, K.; Radu, I.; Detavernier, C., In situ X-ray diffraction study of the controlled oxidation and reduction in the V-O system for the synthesis of VO_2 and V_2O_3 thin films . J. Mater. Chem. C 2015, 3, 11357-11365.
47. Theofanidis, S. A.; Galvita, V. V.; Poelman, H.; Marin, G. B., Enhanced Carbon-Resistant Dry Reforming Fe-Ni Catalyst: Role of Fe. ACS Catal. 2015, 5, 3028-3039.
48. Galvita, V. V.; Poelman, H.; Rampelberg, G.; De Schutter, B.; Detavernier, C.; Marin, G. B., Structural and Kinetic Study of the Reduction of CuO-CeO_2/Al_2O_3 by Time-Resolved X-ray Diffraction. Catal. Lett. 2012, 142, 959-968.
49. Redekop, E. A.; Galvita, V. V.; Poelman, H.; Bliznuk, V.; Detavernier, C.; Marin, G. B., Delivering a Modifying Element to Metal Nanoparticles via Support: Pt-Ga Alloying during the Reduction of Pt/Mg(Al,Ga)O_x Catalysts and Its Effects on Propane Dehydrogenation. ACS Catal. 2014, 4, 1812-1824.
50. Galinsky, N. L.; Shafiefarhood, A.; Chen, Y.; Neal, L.; Li, F., Effect of support on redox stability of iron oxide for chemical looping conversion of methane. Appl. Catal., B 2015, 164, 371-379.
51. Li, K. Z.; Wang, H.; Wei, Y. G.; Zhu, X., Structural Features of Ce-Fe Mixed Oxide and Its Applications in Catalysis. Prog. Chem. 2013, 25, 1691-1702.
52. Zhu, X.; Li, K. Z.; Wei, Y. G.; Wang, H.; Sun, L. Y., Chemical-Looping Steam Methane Reforming over a CeO_2-Fe_2O_3 Oxygen Carrier: Evolution of Its Structure and Reducibility. Energy Fuels 2014, 28, 754-760.
53. Gu, Z. H.; Li, K. Z.; Qing, S.; Zhu, X.; Wei, Y. G.; Li, Y. T.; Wang, H., Enhanced reducibility and redox stability of Fe_2O_3 in the presence of CeO_2 nanoparticles. RSC Adv. 2014, 4, 47191-47199.
54. Moog, I.; Prestipino, C.; Figueroa, S.; Majimel, J.; Demourgues, A., Dual Ce4+/Fe3+ Redox Phenomena into Nanocrystalline $Ce_{1-x}Fe_xO_{2-x/2}$ Solid Solution. J. Phys. Chem. C 2014, 118, 22746-22753.
55. Moog, I.; Feral-Martin, C.; Duttine, M.; Wattiaux, A.; Prestipino, C.; Figueroa, S.; Majimel, J.; Demourgues, A., Local organization of Fe^{3+} into nano-CeO_2 with controlled morphologies and its impact on reducibility properties. J. Mater. Chem. A 2014, 2, 20402-20414.
56. Theofanidis, S. A.; Batchu, R.; Galvita, V. V.; Poelman, H.; Marin, G. B., Carbon gasification from Fe–Ni catalysts after methane dry reforming. Appl. Catal., B 2016, 185, 42-55.

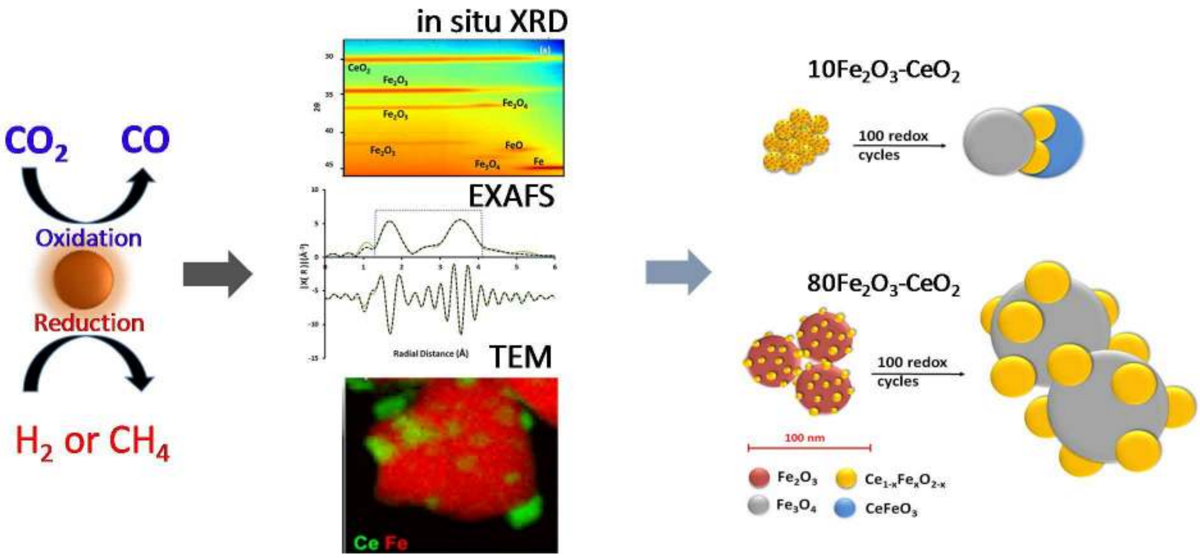
CO2
CO
Oxidation
Reduction
H2 or CH4
in situ XRD
EXAFS
Radial Distance (Å)
TEM
Ce Fe
10Fe2O3-CeO2
100 redox cycles
80Fe2O3-CeO2
100 redox cycles
100 nm
Fe2O3
Fe3O4
Ce1-xFexO2-x
CeFeO3